CHIN. PHYS. LETT. Vol. 38, No. 4 (2021) 047701

Polarization Mechanism in Filled Tungsten Bronze $Ba_4Eu_2Ti_4Nb_6O_{30}$ with Pinched P–E Hysteresis Loops

Lang Zhu(祝朗), Xiao-Li Zhu(朱晓莉)*, Xiao-Qiang Liu(刘小强), and Xiang-Ming Chen(陈湘明)

School of Materials Science and Engineering, Zhejiang University, Hangzhou 310027, China

(Received 20 November 2020; accepted 2 February 2021; published online 6 April 2021)

Pinched P–E hysteresis loops have been observed in filled tungsten bronze $Ba_4Eu_2Ti_4Nb_6O_{30}$, indicating the presence of novel polarization mechanisms. We investigate the evolution of polar order in filled tungsten bronze $Ba_4Eu_2Ti_4Nb_6O_{30}$, together with its dielectric properties over a wide temperature range, from 50 K to 773 K. The temperature dependences of the dielectric properties exhibit two low-temperature dielectric relaxations, at around 300 K (P1), and 100 K (P2), and a high temperature peak at 588 K with no frequency dispersion, indicating the ferroelectric transition temperature T_c. Pinched P–E loops are observed in the temperature range between the low temperature relaxation at P1, and the ferroelectric transition. On cooling, the pinched P–E hysteresis loops open gradually, with increasing remnant polarization (P_r). Two pairs of reversal electric fields indicate two types of polar reversal mechanisms, with an activated energy of 1.41 eV (E_1), and 0.94 eV (E_2), respectively. One corresponds to the field-induced transition from a nonpolar to a polar state, which dominates at a high temperature close to T_c, while the other relates to the reversal of ferroelectric domains which stabilize gradually on cooling. At temperatures below 300 K, the polarization exhibits an evident decrease, probably related to the disruption of the polar order due to the dielectric relaxation at P1.

DOI: 10.1088/0256-307X/38/4/047701

Tungsten bronzes represent one of the most important dielectric and ferroelectric families, containing a large number of functional crystals and materials possessing electro-optic, ferroelectric, pyroelectric, and piezoelectric properties. Moreover, studies of the relationship between structure modulation and ferroelectric properties in this group have yielded a rich supply of physical information, attracting sustained research interest.[1–8] The tetragonal tungsten bronze oxides, with the general formula $A1_2A2_4B1_2B2_8C_4O_{30}$, contain 10 oxygen octahedrals, sharing corners to form channels with triangular, quadrilateral, and pentagonal cross sections. Variable occupancy of the A- and C-sites introduces additional compositional degrees of freedom and structural complexity. When C is unoccupied, the structure may be described as "unfilled", e.g., $(Sr, Ba)_5Nb_{10}O_{30}$,[9] or "filled", e.g., $M_4R_2Ti_4Nb_6O_{30}$ (M denotes an alkali ion, and R denotes a rare earth ion) tungsten bronzes,[10] depending on whether vacancies are present in the A-sites. Compounds with fully occupied A- and C-sites, e.g., $K_6Li_4Nb_{10}O_{30}$ form the "stuffed" tungsten bronze category.[11]

In order to release the A-site-generated strain, structural distortion due to octahedral tilting is common in tetragonal tungsten bronzes, resulting in superstructures with commensurate or incommensurate modulations which determine whether ferroelectric or relaxor ferroelectric behavior appears in tetragonal tungsten bronzes. With respect to filled tungsten bronzes, the radial difference (Δr) between the A1 and A2 site cations plays an important role in ferroelectric behaviors, where compounds with larger Δr tend to show ferroelectric behaviors with commensurate structural modulation, while compounds with relaxor behaviors usually have smaller Δr with incommensurate structural modulation.[12] Recently, a crystal-chemical framework has been proposed to describe the relationship between structural modulations and ferroelectric behavior, considering the balance of two competing factors, both of which can act as the driving force for polar ordering in tungsten bronzes.[13] One is the A site cation size, and the other is the A1 site tolerance factor. Large average A-cation size extends the BO_6 octahedral in the c-axis enhancing polarizability of the d^0 cation, favoring ferroelectric ordering, but with an incommensurate superstructure, due to a modulated tilt pattern. On the other hand, smaller A1 site cations induce a smaller tolerance factor, resulting in larger octahedral tilting with commensurate structural modulation and long-range polar ordering. In the intermediate region, where neither of the two driving forces is strong enough to maintain long-range polar ordering, a local frustrated incommensurate structural modulation causes relaxor behavior.

Under the above framework, novel pinched hysteresis loops are observed in some tungsten bronzes with either relaxor or ferroelectric behaviors, and sys-

Supported by the National Natural Science Foundation of China (Grant Nos. 51790493 and 51961145105).
*Corresponding author. Email: xiaolizi0618@zju.edu.cn
© 2021 Chinese Physical Society and IOP Publishing Ltd

tematic studies of the polarization dynamic and the structural origin are required to investigate this new phenomenon. Pinched hysteresis loops can be observed in ferroelectrics in some cases, including antiferroelectrics with residual polarization at low field, e.g., $AgNbO_3$;[14] the coexistence of a paraelectric phase and a ferroelectric phase during first order ferroelectric transition, which is hardly detectable; defect pinning, which generally occurs in certain perovskite ferroelectrics.[15] In ferroelectric ceramics, the residual oxygen vacancy is the most common defect after high temperature sintering, resulting in defect pinning in the ferroelectric domain. Usually, annealing in an O_2 or N_2 atmosphere will either eliminate or enhance this effect, and could therefore be used as a method to test whether or not the pinched hysteresis loop originates from defect pinning.

However, the mechanism for the pinched hysteresis loops found in tungsten bronzes seems to be quite diverse and unclear. In La and Ti co-doped SBN, $Sr_{0.255}Ba_{0.7}La_{0.03}Nb_{2-y}Ti_yO_{6-\delta}$ with $y = 0.05$, pinched hysteresis loops have been observed in the temperature range between ferroelectric transition and low temperature relaxation (LT1), and attributed to local ordering of an incommensurately modulated antiferroelectric structure within the commensurate ferroelectric matrix.[16] Recently, the occurrence of pinched hysteresis loops in the temperature range between the low-temperature dielectric relaxation and the high-temperature diffuse dielectric peak have been explained as a crossover from a relaxor ferroelectric to a polar but non-ferroelectric state, where large polarization can be established by means of a sufficiently strong electric field.[17] Our recent study presented the pinched loops observed in ferroelectric tetragonal tungsten bronze $Ba_4(Sm/Eu)_2Ti_4Nb_6O_{30}$ below the first order ferroelectric transition, which was associated with a field-induced transition from a non-polar incommensurate to a polar commensurate state, via *in situ* electron diffraction.[18,19]

In this work, we report the detailed evolution of the pinched hysteresis loop in $Ba_4Eu_2Ti_4Nb_6O_{30}$, based on both the applied electric field and temperature. The polarization mechanism is discussed, together with an evaluation of the energy barrier for polarization reversal, the local structure, and the dielectric properties of this material, over a wide temperature range.

The $Ba_4Eu_2Ti_4Nb_6O_{30}$ ceramic was prepared by means of a standard solid-state reaction and sintering process, using reagent grade $BaCO_3$ (99.99%), Eu_2O_3(99.99%), TiO_2 (99.5%), and Nb_2O_5(99.99%) powders as the raw materials. The weighed raw materials were mixed by milling zirconia media in ethanol for 24 h. The mixtures were calcined in high-purity alumina crucibles at 1250℃ in air for 3 h, followed by a second grinding to achieve a homogeneous granulometric distribution. With the addition of organic binders (8 wt% polyvinyl alcohol), the reground powders were then pressed into cylindrical compacts of 12 mm in diameter, at a pressure of 98 MPa. The disks were sintered at 1200–1375℃ in air for 3 h; dense ceramics with relative densities above 96% were obtained when the sintered temperature $T_{\rm sin} \geqq 1300$ ℃, with a maximum relative density of ∼98% being achieved by sintering at 1350 ℃. The SEM image of the dense ceramics is shown in Fig. 1(b), showing the close-packed grains.

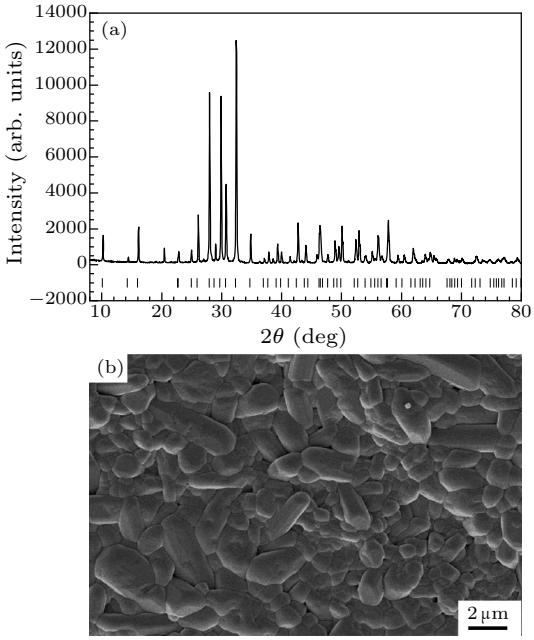

Fig. 1. (a) XRD patterns of $Ba_4Eu_2Ti_4Nb_6O_{30}$ ceramics. (b) SEM of the thermal etching surface of ceramics sintered at 1350℃.

The crystal structure was identified via powder x-ray diffraction (XRD) analysis, with Cu K_α radiation (D/max 3B, Rigaku Co., Tokyo, Japan), at room temperature. The XRD data is shown in Fig. 1(a), and is designated as a tetragonal tungsten bronze structure with a space group of $P4bm$, according to the standard diffraction peaks of JCPDS card #39-0255, shown at the bottom of Fig. 1(a). The low-temperature dielectric characteristics were evaluated using a precision LCR meter (HP 4284 A, Hewlett-Packard Co., PaloAlto, CA) from 50 K to 400 K, while those in the high temperature range (303–773 K) were measured using an LCR meter (Agilent 4294 A, Agilent technologies, Santa Clara, CA). The thermal analysis was performed via differential scanning calorimetry (DSC) (204F1, Netzsch, Phoenix, Arizona) at a heating rate of 20 K/min in Ar. The polarization-field (P–E) hysteresis loops were evaluated from 233 K to 433 K at 10 Hz by a precision materials analyzer (RT Premier Ⅱ, Radient Technologies, Inc., NM).

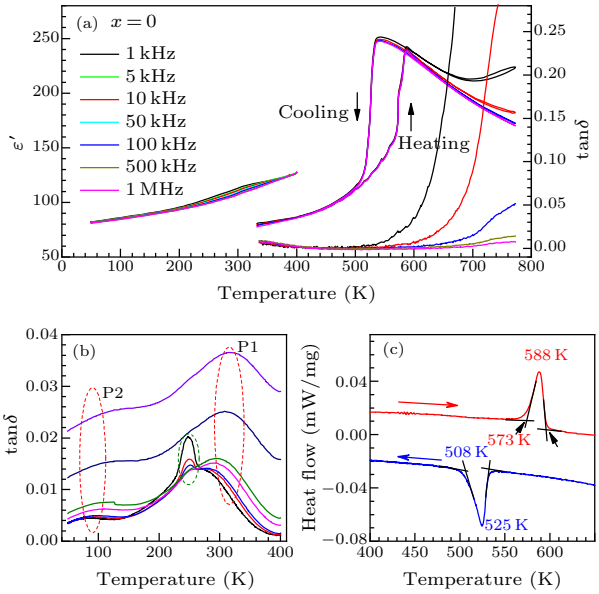

Fig. 2. Temperature dependence of the dielectric property of $Ba_4Eu_2Ti_4Nb_6O_{30}$ ceramics: (a) temperature dependence of dielectric constant from 50–773 K, and dielectric loss from 400–773 K, (b) temperature dependence of dielectric loss from 50–400 K, (c) DSC curves for heating and cooling processes.

According to the temperature dependences of the dielectric constant, and the DSC results on both heating and cooling cycles (see Fig. 2), the ferroelectric transition for $Ba_4Eu_2Ti_4Nb_6O_{30}$ occurs at 588 K on heating, and 525 K on cooling, with a large thermal hysteresis of 63 K, suggesting a first order transition. As shown in the DSC curves for heating and cooling, the ferroelectric transition ends at 508 K on cooling. However, the Curie–Weiss fitting results of the dielectric constant data above T_c give a negative Curie–Weiss temperature T_0 for $Ba_4Eu_2Ti_4Nb_6O_{30}$, indicating that the paraelectric phase could exist as a metastable state even at a very low temperature. As shown in Fig. 2(b), two dielectric relaxations, denoted as P1 and P2 (red circles), could be observed, reflecting polarization fluctuations at lower temperatures. The maximum temperature of P1 increases with increasing temperature, indicating a thermally activated process. The variation of T_m with frequency is shown in Fig. 3, and is fitted to the Vogel Fulcher relation

$$f = f_0 \exp[-E_a/k(T_f - T_m)], \quad (1)$$

where T_f is the static freezing temperature, f_0 is the Debye frequency of the dipoles, E_a is the activation energy, and T_m is the temperature of the permittivity maximum at the applied frequency f.[20] According to the fitting results, the dielectric relaxation P1 has a small activation energy of $E_a = 0.028$ eV, a low Debye frequency of around 1.175×10^7 Hz, and freezes at around 258 K. A small low-frequency anomaly appears at around 250 K, which is ascribed to a dielectric response from the soldering tin used as the electrode welding material for the low-temperature dielectric measurement, and is unrelated to the sample.

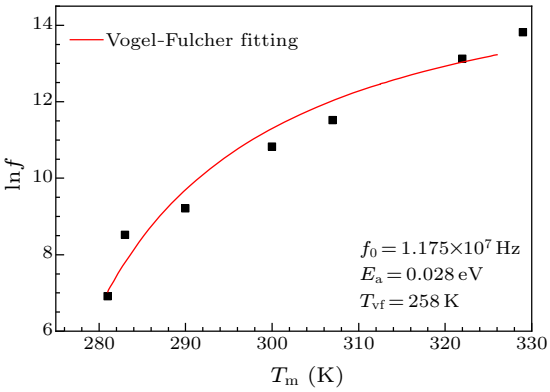

Fig. 3. Frequency dependence of T_m obtained from the dielectric permittivity $[\varepsilon'(T)]$ curve for P1. The red lines indicate the fitting results to the Vogel–Fulcher relation.

For $Ba_4Eu_2Ti_4Nb_6O_{30}$, the high temperature paraelectric phase displays incommensurate structural modulation.[18] Usually, when tungsten bronze ferroelectrics cool down through the Curie temperature T_c, the incommensurate modulation is translated into commensurate modulation, coupling with the paraelectric-to-ferroelectric transition. However, in $Ba_4Eu_2Ti_4Nb_6O_{30}$, below T_c, incommensurate modulation coexists with commensurate modulation, probably due to the fact that the ferroelectric phase coexists with the paraelectric phase for the first order ferroelectric transition due to thermal hysteresis dominating the pinched P–E hysteresis loops, as shown in Fig. 4. Further cooling causes the region of incommensurate modulation to diminish, but remained observable, even at room temperature; as such, the pinched hysteresis loops could also be observed. The coexistence of paraelectric and ferroelectric phases is a theoretical fact; however, it is quite difficult to detect this experimentally. For example, in the ferroelectric tungsten bronze $Ba_4Nd_2Ti_4Nb_6O_{30}$, the incommensurate modulation converts into the commensurate variant immediately at T_c, and no coexistence is detected at any temperature. In $Ba_4Eu_2Ti_4Nb_6O_{30}$, in order to release the large structural strain caused by smaller A1 cations, incommensurate modulation is more stable than that of other tungsten bronze ferroelectrics, and is present far below T_c.

The pinched hysteresis loops appear below the transition temperature, even lower than T_c on cooling. In order to evaluate the evolution of the pinched hysteresis loops, P–E and J–E curves were measured over a temperature range from 233 K to 473 K, as shown in Fig. 4. With increasing temperature close to T_c, the pinched P–E loop looks more and more like the double hysteresis loop, with P_r (the remnant polarization) tending to zero. The variations in P_r and P_m (the maximum polarization) with temperature are

shown in Fig. 5(a). The extension line of P_r versus the T curve indicates a possible zero point for P_r at ~530 K. On cooling, the pinched hysteresis loops open gradually, and the remnant polarization P_r increases. Meanwhile, the shape of the P–E loops becomes less saturated with decreasing temperature, even under a moderately high electric field of 160 kV/cm, thereby indicating a harder polarization reversal at low temperature, and the maximum polarization P_m decreases gradually on cooling.

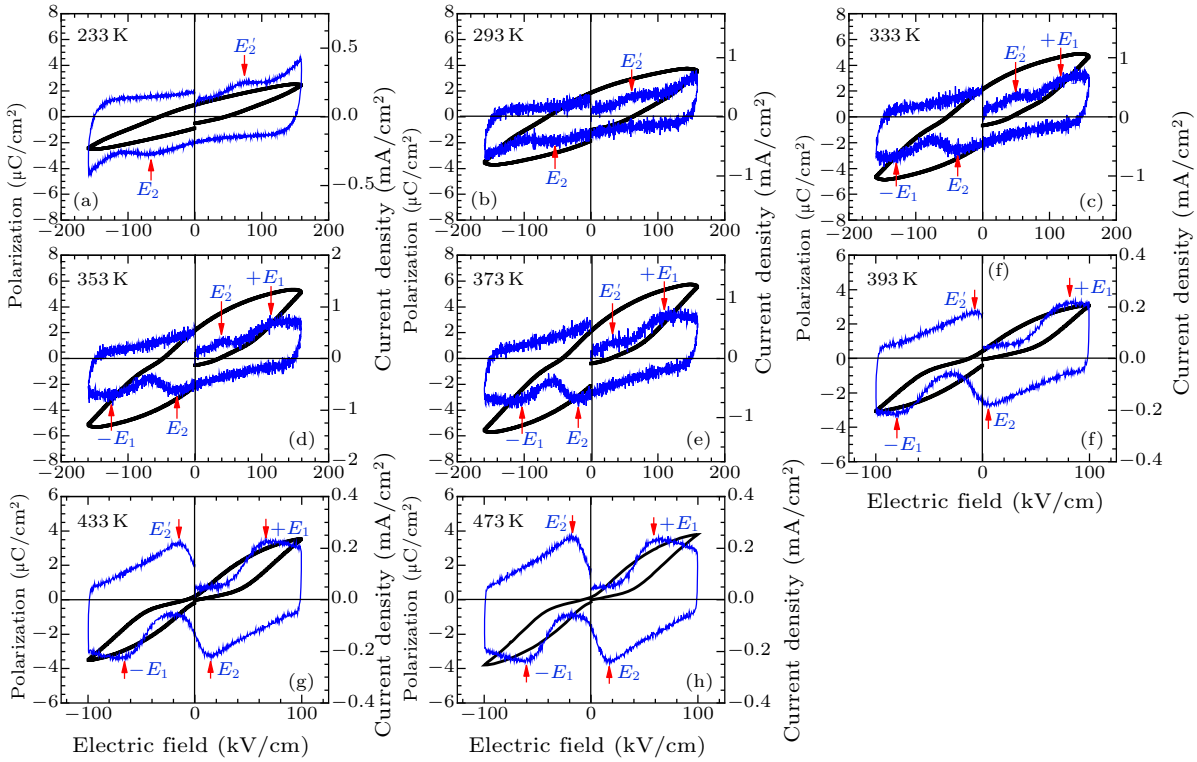

Fig. 4. Evolution of the pinched Polarization-electric field (P–E) loops on heating, and corresponding current density-electric field (J–E) curves of $Ba_4Eu_2Ti_4Nb_6O_{30}$ ceramics with temperature.

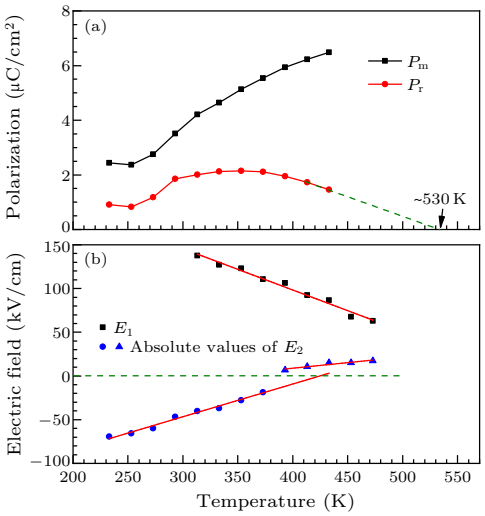

Fig. 5. Temperature dependences of (a) maximum polarization P_m, and remnant polarization P_r, (b) two polarization switching fields (E_1 and E_2), fitted to the Vopsaroiu model, for $Ba_4Eu_2Ti_4Nb_6O_{30}$.

Two pairs of reversal electric fields, denoted as E_1 and E_2, can be obtained from the J–E curves of Fig. 4. Based on our previous work, the pinched P–E hysteresis loops in $Ba_4Eu_2Ti_4Nb_6O_{30}$ originate from a field-induced transition from a nonpolar incommensurate structural modulation to a polar commensurate modulation. Therefore, E_1 represents the onset electric field from the nonpolar to the polar state, and E_2 is the depolarization electric field. As shown in Fig. 5(b), the values of reversal electric field E_1 increase almost linearly on cooling, whereas the values of E_2 decrease, changing from positive to negative when the temperature drops from 393 K to 373 K, together with an obvious change in the curve slope. The variation of E_2 with temperature is clearly depicted in Fig. 5(b). At higher temperatures, E_2 appears at the fourth quadrant with a positive value, and moves into the third quadrant on cooling.

The polarization dynamics and non-equilibrium switching processes in ferroelectrics can be analyzed using the Vopsaroiu model,[21,22] and the relationship between E_c and T can be written as

$$E_c(T) = \frac{W_B}{P_s} - \frac{k_B T}{P_s V^*} \ln\left(\frac{v_0 t}{\ln 2}\right), \tag{2}$$

where W_B is the energy barrier per unit volume for the polarization reversal, V^* is the critical domain volume of the elementary nucleation site, P_s is the spontaneous polarization at zero applied field, v_0 is the phonon frequency, and t is the measurement time.

This model predicts that E_c measured at constant time varies linearly versus T with a negative slope. W_B and V^* can be extracted from the linear fitting results for a plot of E_c against T. Therefore, the variations of E_1 and E_2 vs T are fitted to the above equation as $E(T) = a - bT$, where $a = W_B/P_m$ and $b = k_B(V^*P_m)^{-1}\ln(v_0 t/\ln 2)$, with the fitting lines indicated by the red lines in Fig. 5(b). Here, $t = 0.1$ s (i.e., a frequency of 10 Hz), $k_B = 1.381\times10^{23}$ J/K, and $v_0 = 10^{12}$ Hz. To obtain W_B and V^*, P_s is required. In the Vopsaroiu model, P_s is defined as reversible polarization, or spontaneous polarization. Here, for simplicity, the maximum polarization P_m is used in place of P_s.

Table 1. Calculated parameters using the experimental results shown in Fig. 5(b) and the simulation using Eq. (1).

	a (kV/cm)	b (kV/cm·K)	$W_B(10^{24}\,\mathrm{V/m^3})$	$V^*(10^{-25}\,\mathrm{m^3})$	W_BV^* (eV)
E_1 (313–433 K)	271.2	0.427	7.13–10.98	1.97–1.28	1.41
E_2 (233–433 K)	158.9	0.374	2.41–6.43	3.89–1.46	0.94

In the temperature regions where E_1 and E_2 (the negative part) were detected, the maximum polarization varies with the measured temperature. Since fixed values for the parameters a and b are determined by the linear fitting of the experimental data to the Vopsaroiu model, this means that W_B and V^* are connected and balanced with the maximum polarization. Therefore, the energy barrier, or the activation energy per critical volume, W_BV^*, is independent of P_s. The corresponding relationships can be derived from the Vopsaroiu model as follows:

$$W_B = aP_s, \tag{3}$$

$$V^* = -\frac{1}{bP_s}k_BT\ln\left(\frac{v_0t}{\ln 2}\right), \tag{4}$$

$$W_BV^* = k_B\frac{a}{b}\ln\left(\frac{v_0t}{\ln 2}\right). \tag{5}$$

The calculated W_BV^* value is 1.41 eV for E_1, and 0.94 eV for E_2, which is quite large compared with other normal ferroelectrics. For example, the values calculated for $Pb(Zr_{0.52}Ti_{0.48})O_3$[21] and $Ba_4Sm_2Ti_4Ta_6O_{30}$[23] are $V^* \sim 3\times10^{-25}\,\mathrm{m^3}$ and $W_BV^* \sim 0.7$ eV, respectively.

For a P–E hysteresis loop, coercive electric field E_c reflects the degree of difficulty in achieving polarization reversal in ferroelectric domains. The pinched loop includes two cycles of polarization and depolarization between the incommensurate and commensurate states, and the degree of difficulty of these polarization and depolarization processes can be evaluated using $\Delta E = E_1 - E_2$. On cooling, the incommensurate state becomes more unstable, and therefore the depolarization from the polar state back to the nonpolar incommensurate state tends to be more difficult. The opposite variation of E_1 and E_2 reflects the increasing difficulty of the depolarization transition.

On the other hand, when E_2 becomes negative, E_2' becomes positive. Based on the P–E and J–E loops shown in Fig. 4, two current peaks exist in one quadrant (E_2' and E_1 in the first quadrant, E_2 and $-E_1$ in the fourth quadrant). This phenomenon indicates the polarization reversal of two types of polar structure. Below T_c, in addition to the field-induced transition, the main polar structure in $Ba_4Eu_2Ti_4Nb_6O_{30}$ should consist of stable ferroelectric domains. These two mechanisms compose the polar structure at lower temperature. At temperatures below T_c, the polar commensurate phase is stable, and the incommensurate region is quite diluted; therefore the pinched shape is inconspicuous, and the P–E loop primarily reflects the reversal of the ferroelectric domain. It should be noted that the P–E loops below 300 K are much less saturated, even under a very high electric field, more closely resembling the characteristics of a relaxor rather than a ferroelectric state, suggesting that the low temperature relaxation observed in the dielectric curves disturbs the long-range polar order.

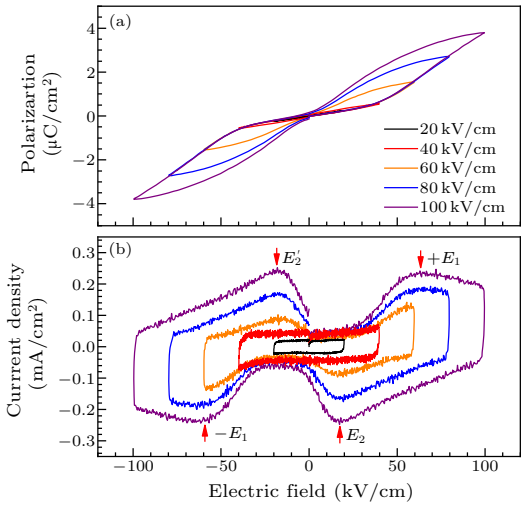

Fig. 6. (a) Pinched Polarization-electric field (P–E) loops of $Ba_4Eu_2Ti_4Nb_6O_{30}$ ceramics, measured at 433 K for different applied electric fields, and (b) corresponding current density-electric field (J–E) curves.

With increasing temperature, the incommensurate area increases, and the electric field-induced transition from the non-polar incommensurate state to the polar commensurate state dominates the shape of the P–E hysteresis loop, making the pinched loop more obvious with decreasing P_r. When $T \to T_c$, P_r is close to zero at ~530 K, as extracted from Fig. 5(a), and values of both the current peak E_1 (the electric field from incommensurate to commensurate state, first quad-

rant) and E_2 (the reverse field from commensurate to incommensurate state, fourth quadrant) are positive. On cooling, E_2 shifts rapidly to the left and into the third quadrant, while the value changes from positive to negative, and the absolute value first decreases and then increases, indicating that the reverse electric field goes through two different stages: one with a positive value, the other with a negative value.

Figure 6 shows the evolutions of P–E and J–E curves with increasing applied electric field, measured at 473 K, with the following results: firstly, E_2 is activated at a lower electric field above 60 kV/cm, as compared to E_1, which is detected at fields above 80 kV/cm. Secondly, the positions of the four current peaks are stable with applied electric field at a certain temperature, indicating that the polarization reversals are primarily thermally activated processes.

In summary, we have examined the first order ferroelectric transition, low temperature dielectric relaxations, and evolution of the polarization mechanism over a wide temperature range, for filled tungsten bronze ferroelectric $Ba_4Eu_2Ti_4Nb_6O_{30}$, revealing a novel pinched P–E hysteresis loop. Two types of polar structure dominate the polarization reversal. At higher temperatures below T_c, the electric field-induced transition from the nonpolar incommensurate state to the polar commensurate state leads to the obvious pinched P–E loops. The pinched P–E loops open gradually on cooling, and the stabilized polar domains dominate the polarization reversal. At temperatures below room temperature, the polar order is disrupted by the low temperature dielectric relaxation P1, resulting in decreasing polarization.

References

[1] Yang Z J, Zhu X L, Liu X Q and Chen X M 2018 *Appl. Phys. Lett.* **113** 142902

[2] Yang Z J, Feng W B, Zhu X L, Liu X Q and Chen X M 2019 *J. Am. Ceram. Soc.* **102** 4721

[3] Yang Z J, Zhu X L, Liu X Q and Chen X M 2020 *Appl. Phys. Lett.* **117** 122902

[4] Feng W B, Zhu X L, Liu X Q and Chen X M 2017 *J. Mater. Chem. C* **5** 4009

[5] Feng W B, Zhu X L, Liu X Q, Fu M S, Ma X, Jia S J and Chen X M 2018 *J. Am. Ceram. Soc.* **101** 1623

[6] Feng W B, Zhu X L, Liu X Q and Chen X M 2018 *Appl. Phys. Lett.* **112** 262904

[7] Feng W B, Zhu X L, Liu X Q and Chen X M 2018 *J. Appl. Phys.* **124** 104102

[8] Feng W B, Zhu X L, Liu X Q, and Chen X M 2019 *Appl. Phys. Lett.* **114** 082902

[9] Glass A M 1969 *J. Appl. Phys.* **40** 4699

[10] Stennett M C, Reaney I M, Miles G C, Woodward D I, West A R, Kirk C A and Levin I 2007 *J. Appl. Phys.* **101** 104114

[11] Abrahams S C, Jamieson P B and Bernstein J L 1971 *J. Chem. Phys.* **54** 2355

[12] Zhu X L, Li K and Chen X M 2014 *J. Am. Ceram. Soc.* **97** 329

[13] Zhu X, Fu M, Stennett M C, Vilarinho P M, Levin I, Randall C A, Gardner J, Morrison F D and Reaney I M 2015 *Chem. Mater.* **27** 3250

[14] Tian Y, Jin L, Zhang H F, Xu Z, Wei X Y, Politova E D, Stefanovich S Y, Tarakina N V, Abrahams I and Yan H X 2016 *J. Mater. Chem. A* **4** 17279

[15] Tan Q, Li J X and Viehland D 1999 *Appl. Phys. Lett.* **75** 418

[16] Amorin H, Perez J, Fundora A, Portelles J, Guerrero F, Soares M R, Martinez E and Siqueiros J M 2003 *Appl. Phys. Lett.* **83** 4390

[17] Gardner J, Yu F J, Tang C, Kockelmann W, Zhou W Z and Morrison F D 2016 *Chem. Mater.* **28** 4616

[18] Li K, Zhu X L, Liu X Q, Ma X, Fu M S, Kroupa J, Kamba S and Chen X M 2018 *NPG Asia Mater.* **10** 71

[19] Li C, Hong J S, Huang Y H, Ma X, Fu M S, Li J, Liu X Q and Wu Y J 2019 *Appl. Phys. Lett.* **115** 082901

[20] Glazounov A E and Tagantsev A K 1998 *Appl. Phys. Lett.* **73** 856

[21] Vopson M M, Weaver P M, Cain M G, Reece M J and Chong K B 2011 *IEEE Trans. Ultrason. Ferroelectr. Freq. Control* **58** 1867

[22] Vopsaroiu M, Blackburn J, Cain M G and Weaver P M 2010 *Phys. Rev. B* **82** 024109

[23] Zhu X L and Chen X M 2016 *Appl. Phys. Lett.* **108** 152903